Article:

Stone, Andrew P., Rand, Emma, Thornes, Gabriel et al. (4 more authors) (2024) Extracellular matrices of stromal cell subtypes regulate phenotype and contribute to the stromal microenvironment in vivo. Stem Cell Research and Therapy. 178. ISSN 1757-6512

https://doi.org/10.1186/s13287-024-03786-1

Stone *et al. Stem Cell Research & Therapy* (2024) 15:178
https://doi.org/10.1186/s13287-024-03786-1

Stem Cell Research & Therapy

RESEARCH Open Access

Extracellular matrices of stromal cell subtypes regulate phenotype and contribute to the stromal microenvironment in vivo

Andrew P. Stone[1,2*], Emma Rand[1], Gabriel Thornes[1], Alasdair G. Kay[1], Amanda L. Barnes[1], Ian S. Hitchcock[1] and Paul G. Genever[1]

Abstract

Background Bone marrow stromal cells (BMSCs) are highly heterogeneous, which may reflect their diverse biological functions, including tissue maintenance, haematopoietic support and immune control. The current understanding of the mechanisms that drive the onset and resolution of heterogeneity, and how BMSCs influence other cells in their environment is limited. Here, we determined how the secretome and importantly the extracellular matrix of BMSCs can influence cellular phenotype.

Methods We used two immortalised clonal BMSC lines isolated from the same heterogeneous culture as model stromal subtypes with distinct phenotypic traits; a multipotent stem-cell-like stromal line (Y201) and a nullipotent non-stem cell stromal line (Y202), isolated from the same donor BMSC pool. Label-free quantitative phase imaging was used to track cell morphology and migration of the BMSC lines over 96 h in colony-forming assays. We quantified the secreted factors of each cell line by mass spectrometry and confirmed presence of proteins in human bone marrow by immunofluorescence.

Results Transfer of secreted signals from a stem cell to a non-stem cell resulted in a change in morphology and enhanced migration to more closely match stem cell-like features. Mass spectrometry analysis revealed a significant enrichment of extracellular matrix (ECM) proteins in the Y201 stem cell secretome compared to Y202 stromal cells. We confirmed that Y201 produced a more robust ECM in culture compared to Y202. Growth of Y202 on ECM produced by Y201 or Y202 restored migration and fibroblastic morphology, suggesting that it is the deficiency of ECM production that contributes to its phenotype. The proteins periostin and aggrecan, were detected at 71- and 104-fold higher levels in the Y201 versus Y202 secretome and were subsequently identified by immunofluorescence at rare sites on the endosteal surfaces of mouse and human bone, underlying CD271-positive stromal cells. These proteins may represent key non-cellular components of the microenvironment for bona-fide stem cells important for cell maintenance and phenotype in vivo.

Conclusions We identified plasticity in BMSC morphology and migratory characteristics that can be modified through secreted proteins, particularly from multipotent stem cells. Overall, we demonstrate the importance of specific ECM proteins in co-ordination of cellular phenotype and highlight how non-cellular components of the BMSC microenvironment may provide insights into cell population heterogeneity and the role of BMSCs in health and disease.

---

*Correspondence:
Andrew P. Stone
Andrewstone@brandeis.edu
Full list of author information is available at the end of the article

Keywords Extracellular matrix, Bone marrow stromal cell, Cellular heterogeneity, Secretome, Stromal microenvironment

Background

The bone marrow microenvironment is complex, with interplay and heterotypic signalling between haematopoietic and non-haematopoietic compartments [1, 2]. The study of bone marrow stromal cells (BMSCs) within this environment has often focused on how BMSCs interact and communicate with other cell types, with particular attention to their role in skeletal homeostasis, haematopoietic control and immunomodulation [2–7].

We and others have previously reported considerable heterogeneity in stromal populations, in terms of morphological and functional characteristics [8, 9]. Work in both mice and humans has provided evidence for a carefully co-ordinated developmental tree of BMSCs that is critical to skeletal lineage differentiation and bone marrow architecture [10, 11]. Recent developments in single-cell profiling have facilitated the interrogation of stromal diversity, with several reports of complex, heterogeneous subsets [12–18]. However, there has been little work to investigate how the phenotype of these stromal subsets is coordinated and how they interact with one another to influence tissue architecture, remodelling and inflammatory responses in healthy and disease states. BMSCs are capable of mediating both pro- and anti-inflammatory effects, and ample evidence suggests a correlation between cellular morphology and function [19–21].

We previously reported the development of a panel of human telomerase reverse transcriptase (hTERT) immortalised clonal BMSC lines that partially model stromal heterogeneity in bone marrow [22]. These include the Y201 line which exhibits classical stem cell-like tri-potent differentiation capacity, and the Y202 BMSC line, that is nullipotent and has pro-inflammatory characteristics. Both of these BMSC lines express cell surface proteins described by Dominici et al. as well as the commonly reported marker leptin receptor (LEPR) [23]. However, Y201 and Y202 BMSCs display considerable variation in morphology, migration, transcriptional profiles and function, highlighting a need for further refinement of stromal identity [24].

Heterogeneous stromal cells are likely to reside in subtype-specific locations in vivo and their local environment will have considerable influence on cell phenotype. There is also significant interest in the role that BMSCs play in the haematopoietic niche, therefore defining the composition of specific niche environments would aid understanding of their function, in particular the contribution of non-cellular components such as cytokines and extracellular matrix (ECM). There is also specific relevance for understanding disease pathologies; for example, de Jong et al. showed evidence for involvement of different subsets of BMSCs in multiple myeloma [25].

Here we used our immortalised BMSC lines to examine phenotypic stability. We demonstrate that heterogeneous BMSC sub-populations are inherently plastic both in terms of cell morphology and migratory characteristics, that this plasticity is inducible through the exposure to secreted factors from different stromal subsets, and that these subsets produce distinct ECMs at varying quantities which may contribute to phenotype. Our findings add to our understanding of the mechanisms that determine the onset and resolution of heterogeneity in different cell and tissue contexts. Furthermore, we demonstrate differential contribution of BMSC subsets to ECM production in vitro and highlight candidate components of a putative stem cell-supporting microenvironment in vivo, which will prove important for understanding disease development, identification of functional subpopulations and for production of ex vivo expanded cells for therapeutic applications.

Methods

Cell culture

Y201 and Y202 BMSC lines were cultured in complete medium (Dulbecco's Modified Eagle Medium (DMEM) containing 10% foetal bovine serum (FBS), 100units/ml penicillin and 100 μg/ml streptomycin) and incubated at 37 °C in a 95% air/5% CO_2 atmosphere. Cells were passaged using trypsin-EDTA on reaching 70–80% confluency. hTERT cell lines have a consistent population doubling time of approximately 25 h [24]. All work involving human samples was approved by the University of York, Department of Biology Ethics Committee. Primary human BMSCs were isolated from femoral heads obtained with informed consent during routine hip replacement or as explant cultures from the tibial plateau after routine knee replacement surgery.

Conditioned media collection for secretome analysis and functional assays

Conditioned media was collected from 2× T175 flasks of Y201 and Y202 BMSC lines. Cells were grown to ~80% confluency before washing 2× with PBS, 17 ml of serum-free DMEM was added to the flasks and incubated as normal for 24 h. Medium was collected and then centrifuged at 300 g to remove any large cell debris.

For functional assays, medium was stored at − 80 °C until required. For proteomic analyses, the medium was concentrated in 3kD-MWCO tubes (GE Healthcare) at 4500 g until concentrated to ~ 1 ml in volume. Media were stored at − 80 °C until required.

Preparation of MSC-derived ECM

ECM was prepared from in vitro cell cultures using a protocol adapted from Ng et al. [26]. Cells were seeded at 1000 cells/cm^2 in 6-well plates or on 13 mm glass coverslips and allowed to grow for 14 days where they reached confluency, in contrast to normal culture. For days 1–7, cells were grown in complete medium and for days 8–14 this medium was supplemented with 50 µM L-ascorbic acid to enable matrix accumulation (Sigma-Aldrich). Medium changes were performed every 3 days. On day 14, medium was aspirated and cells were removed from the deposited ECM by incubation (5 min, room temperature) with 20 mM ammonium hydroxide with 0.5% Triton X-100 in PBS and gentle agitation every minute. Plates were washed 1× with PBS and 3× with sterile dH$_2$O after cell clearing. Matrices were dried in a sterile laminar flow cabinet before storing at 4 °C wrapped in parafilm for up to 1 month.

Scanning electron microscopy (SEM)

ECM samples were fixed for 30 min in a mixture of 4% paraformaldehyde (PFA) + 2.5% glutaraldehyde in 100 mM phosphate buffer (pH 7.0) at room temperature. Samples were washed twice for 10 min each with phosphate buffer before secondary fixation with 1% osmium tetroxide for 30 min at room temperature. Samples were washed twice with phosphate buffer for 10 min, then dehydrated in an ethanol series of 25%, 50%, 70%, 90% and 3 × 100% for 15 min at each stage. Samples were covered with hexamethyldisilazane for 15 min before aspirating and allowing to air dry. Samples were imaged with a JEOL 7800F Prime.

Focused ion beam scanning electron microscopy (FIB-SEM)

Samples were prepared for FIB-SEM by fixing in 2.5% glutaraldehyde in 100 mM phosphate buffer for 1 h before 3 × 15 min washes with phosphate buffer. A secondary fixation with 1% OsO$_4$ in 100 mM phosphate buffer was performed for 1 h before 3 × 5 min washes with ddH$_2$O. Samples were then blocked in 1% uranyl acetate in ddH$_2$O for 1 h. Samples underwent dehydration in an ethanol series with 15 min in 30%, 50%, 70%, 90% and 2 × 15 min in absolute ethanol. The samples were then washed 2 × 5 min in epoxy propane before infiltrating with Epon-araldite resin (Epon 812, Araldite CY212) overnight. Excess resin was removed by spinning coverslips at 1000 g before the resin was polymerised at 60 °C for 48 h. Prior to FIB milling, carbon coating was evaporated onto the matrix surface to provide a conductive sheath. The underlying film is protected from the destructive effect of the ion beam by the deposition of a thin (2–3 µm) layer of nanocrystalline platinum and amorphous carbon. The Pt atoms provide a high-Z barrier to unwanted Ga ion exposure. Milling into the film commences with a high current ion probe (7 nA) that produces a deep, triangular trench to a depth of several micrometres. A series of 'cleaning scans' were executed with smaller ion probe currents (1 nA, 300 pA, 50 pA, all at 30 keV) to remove thin layers of damaged surface material. This exposed the interfaces between the substrate, the thin film and the deposited carbon and platinum layers. Finally, the sample could be tilted to ensure that optics were as close to the milled surface as possible for imaging.

Proteomic analysis

Concentrated whole secretome samples were added to 8 M urea with 20 mM HEPES, 1 mM sodium orthovanadate, 1 mM β-glycerophosphate and 2.5 mM sodium pyrophosphate (Sigma-Aldrich). Protein was in-solution reduced and alkylated before digestion with a combination of Lys-C and trypsin proteases. Resulting peptides were analysed over 1 h LC–MS acquisitions using an Orbitrap Fusion. Peptides were eluted into the mass spectrometer from a 50 cm C18 EN PepMap column. Three biological replicates for each cell line were run. Tandem mass spectra were searched against the human subset of the UniProt database using Mascot and peptide identifications were filtered through the Percolator algorithm to achieve a global 1% false discovery rate (FDR). Identifications were imported back into Progenesis QI and mapped onto MS1 peak areas. Peak areas were normalised to total ion intensity for all identified peptides. Relative protein quantification was performed using relative peak areas of non-conflicting peptides. Relative fold differences and associated p-values for differential abundance were calculated in Progenesis QI.

Bioinformatic analyses

Proteins were annotated for involvement in the Matrisome using the MatrisomeDB database at https://sites.google.com/uic.edu/matrisome/home [27]. Chi-squared tests were performed in Graphpad Prism 9.

Lists of significantly more abundant genes and proteins were analysed for pathway enrichment against the curated Kyoto Encyclopedia of Genes and Genomes (KEGG) database using the Molecular Signatures Database website on version 7.2 [28–30]. Enrichment was performed for significantly different protein lists and results filtered to exclude terms with FDR corrected *p*-values (q) of >0.05. To minimise the effect of confounding and relatively uninformative terms, a filter excluded protein-sets containing more than 500 proteins. Where *p*-values for enriched pathways were the same, samples were ordered by the MSigDB k/K ratio where k = the number of proteins identified in the protein-set and K = the total number of proteins in that set. Enrichments were presented in bar-charts generated in Graphpad Prism. Cytoscape was used for visualisation of cellular location of proteins from secretomics [31].

Ptychography, cell tracking and image analysis

For cell migration and morphology analysis cells were seeded as 6-well colony-forming unit fibroblastic (CFU-F) assays and ptychography, a form of quantitative phase imaging, was performed using a Phasefocuslivecyte for live cell tracking analysis. Images were taken at 20–26-min intervals for 96 h. Images were first processed with a rolling ball algorithm before smoothing was applied to remove low frequency noise. Points of maximal brightness, indicating areas of high phase-contrast corresponding to cell nuclei, were identified in the smoothed image and were used as seeding points for the identification of individual cells. Seed points were consolidated where points that did not change in pixel intensity within a threshold were removed, this enabled removal of multiple seed points in a single cell. Thresholding and segmentation levels were set to define the cell area against the background. This processing pipeline was applied to all images in an experiment. The output images then allowed tracking of cells with the Phasefocus cell tracking algorithm and using a spatial and temporal dot plot, along with quantification of various morphological metrics such as dry-mass, area, width and length. The tracking algorithm used has been shown to be comparative to other methodologies [32]. Small debris was removed by an exclusion gate removing objects that were less than 250 pg in dry mass and less than 1000 μm^2. Large doublets and debris were excluded with an area over 25,000 μm^2. Manual removal of debris was also performed by visual assessment. To be included in analyses, cells had to be tracked for a minimum of 20-frames. Cell morphology and migration was quantified using the Phasefocus analysis platform and statistical tests performed in Graphpad Prism. Rose plots were generated using the mTrackJ plugin in ImageJ [33]. The image analysis program CellProfiler was used to generate a pipeline to assess the morphological characteristics of BMSCs [34]. This pipeline was subsequently used to categorise different BMSC subtypes into subgroups of Y201, Y202 or a group of cells that were between categories.

CFU-F assays and image analysis

For CFU-F assays, cells were seeded at 10 cells/cm^2 in 6-well plates using DMEM supplemented with 20% Hyclone FBS containing 100units/ml penicillin, 100 μg/ml streptomycin. Conditioned medium for use in the CFU-F assays was collected from Y201 and Y202 MSCs by incubating in serum-free medium at ~ 80% confluency for 24 h before collecting media, centrifuging at 300 g to remove cell debris, and counting the number of cells. The conditioned medium was then diluted with additional serum-free DMEM to give 12 ml conditioned media/million cells. This medium was then supplemented with a final concentration of 20% Hyclone FBS for use in CFU-F assays. For CFU-Fs, primary cells and cell lines were seeded in unconditioned Hyclone medium before media changes were performed every 4 days post-seeding and plates were fixed and stained at day 10 for cell lines and day 14 for primary cell. Plates were stained with (0.05% crystal violet + 1% formaldehyde + 1% methanol in PBS) for imaging or were washed 1 × with PBS and the cells lysed with 350 μL of RA1 cell lysis buffer (Machery-Nagel) + 3.5 μL β-mercaptoethanol for every 3 wells. Well plates were air dried before scanning on an Epson Perfection 4990 Photo scanner at 1200 dpi.

CellProfiler pipeline

A CellProfiler pipeline was subsequently developed to detect and measure colonies accurately [35]. The scanned image was loaded into CellProfiler and converted to a greyscale image using the ColorToGrey module, splitting the image into Red, Green and Blue channels. The Blue channel was then thresholded to 0.99 to include all features identified as completely black. Well edges were identified as primary objects of size 1000–2000-pixel units in diameter and with a manual threshold of 0.99 to include all features, this reproducibly identified the well edges as primary objects. In order to fit this as a complete circle a grid was defined using DefineGrid and then true circles were placed using the IdentifyObjectsinGrid module. The circle was shrunk by 10 pixels in diameter to prevent running over the edge of the well. The UnmixColors module was used to create an image without any Blue absorbance (Red and Green absorbance of 1, Blue absorbance of 0). The area of this image outside of the wells was cropped using the 10 pixel shrunken circles. Illumination correction was calculated (block size 20, median filter and Object size filter with median object size of 80 pixels), and applied by subtraction. The edges of features were enhanced using the Sobel method in the EnhanceEdges module which identified cells that had dispersed away from an otherwise tight colony. The distance of these cells was then closed using a Closing module in a

Diamond shape with a reach of 10 pixels. Colonies were subsequently detected by an IdentifyPrimaryObjects module with typical diameter between 60 and 800 pixels and using the RobustBackground with a Mode averaging. Manual correction of colony detection could then be applied in CellProfiler. Resultant colonies were measured for size and shape characteristics and used as a mask to analyse other features of the colonies such as intensity.

Senescence associated beta galactosidase assay

The presence of senescence associated beta galactosidase was determined by culturing Y201 and Y202 for 24-h prior to fixation and subsequent enzymatic activity assay using an established protocol [36].

Osteogenic differentiation

For osteogenic differentiation, cells were seeded at 1000 cells/cm^2 in 24-well plates in complete medium (described above) to allow expansion of cells and spreading over the ECM layer. Cells were left to grow until reaching confluency before supplementing medium with 50 μg/mL L-ascorbic acid-2-phosphate, 5 mM β-glycerophosphate and 10 nM Dexamethasone to produce osteogenic media. Fresh osteogenic media changes were performed every 3–4 days. Time-points were collected at days 0, 7, 14 and 21. At each timepoint, medium was aspirated and the cells washed once with PBS. Cells were fixed with 4% PFA in PBS for 5 min at room temperature. Cells were then washed 3× with PBS before covering in PBS and storing at 4 °C until staining. At assay endpoint all fixed plates were washed once with PBS before addition of 40 mM Alizarin Red S in distilled water adjusted to pH 4.2 with hydrochloric acid for 20 min at room temperature. After staining, cells were washed 3× with PBS and subsequently with gently running tap water to remove non-specific staining. Plates were left to air-dry before scanning on an Epson Perfection 4990 Photo scanner at 1200dpi.

Focal adhesion immunostaining assessment

Y201 and Y202 cells were plated onto glass coverslips left to adhere for 24 h. Cells were fixed briefly in 4% methanol-free PFA in PBS before washing 3× with PBS. Cells were permeabilised in 0.1% Triton X-100 in PBS for 30 min and washed 3× with PBS. Cells were then blocked for 30 min with 10% goat serum in PBS. Anti-vinculin antibody (Sigma-Aldrich) was added in 1% BSA and incubated at room temperature for 1 h. Cells were washed 3× with PBS before Goat anti-mouse Alexafluor-488 conjugated secondary antibody (ThermoFisher) was added along with Cruzfluor-594 conjugated phalloidin (Santa Cruz) for 45 min in PBS followed by another 3× washes. Nuclei were counterstained with 0.2 μg/ml DAPI for 10 min before rinsing briefly in distilled water and leaving to air-dry. Coverslips were mounted onto a microscope slide with Prolong gold antifade (ThermoFisher).

Slides were imaged on a Zeiss LSM880 or LSM780 microscope. Focal adhesion sizes were quantified using ImageJ. All antibody manufacturers, clones and dilutions can be found in supplementary Table S1.

Immunofluorescence of mouse femurs

Female 8–12 week old C57Bl/6 mice used in this study were kept on a 12-h day/night cycle with free access to water. Animals were euthanised by schedule 1 method of asphyxiation with rising concentration of CO$_2$, followed by cervical dislocation under approval of a UK home office project license. Femurs were collected and fixed in 4% PFA in PBS for 24 h followed by decalcification in 10% EDTA in PBS pH 7.5 for 24 h. Bones were then transferred to 30% sucrose in PBS for 24 h before freezing in optimal cutting temperature (OCT) compound on a dry ice and ethanol slurry. Sections were cut to 8 μm thickness on a Bright OTF5000 cryostat and collected on Superfrost plus slides (ThermoFisher). Sections were blocked in 10% goat serum + 0.1% Tween-20 in PBS for 45 min before addition of primary antibodies in 1% Bovine Serum Albumin + 0.05% Tween-20 and left overnight at 4 °C. Sections were washed 3 times for five minutes with PBS before adding all secondary antibodies in PBS for 1 h at room temperature. Antibody manufacturer and dilution details are provided in supplementary Table S1. Three five-minute washes were performed before staining for 10 min with 0.2 μg/ml DAPI in PBS (Sigma). Slides were rinsed in dH$_2$O and dried before mounting a glass coverslip with Prolong Gold antifade mounting medium (Invitrogen). Images were taken on LSM880 or LSM780 confocal microscopes or a AxioScan slidescanner (Zeiss). Positive expression was confirmed following comparison with controls labelled with isotypes to primary antibody followed by secondary antibody labelling. Experiments have been reported in accordance with the ARRIVE 2.0 guidelines.

Immunofluorescence of human bone

Human femoral heads from routine hip and knee replacements were donated following informed consent from Clifton Park Hospital under ethical approval from the local NHS Research Ethics Committee and the University of York, Department of Biology Ethics Committee. A CleanCut bone saw (deSoutter medical) was used to cut femoral heads which were then dissected into roughly 1 cm^3 pieces using a scalpel. Processing steps were carried out at 4 °C. Bone pieces were fixed in 4% PFA for 24 h. After fixation, samples were washed once with PBS before decalcifying for 48 h in 10% EDTA in

PBS at pH 7.5. Bone pieces were cryoprotected by submerging in 30% sucrose in PBS for 24 h before cutting into smaller pieces with a scalpel and embedding in OCT on a dry ice ethanol slurry. Sections were cut at 10 µm on a Bright OTF5000 cryostat with a tungsten-carbide blade and collected on Superfrost plus slides (ThermoFisher). Immunofluorescent staining was then performed as for the sections of mouse bone described above. All antibody manufacturers, clones and dilutions can be found in supplementary Table S1.

Results

Heterogeneous BMSCs have distinct morphologies and migratory characteristics

Through CFU-F and related assays our group and others have identified morphologically distinct BMSC subtypes in primary donor populations. The morphology of colonies and of individual cells within colonies could reflect and/or be predictive of biological function. The immortalised BMSC lines, Y201 and Y202, have different cellular morphologies; Y201 cells have a typical elongated, bipolar stromal morphology, whereas Y202 cells are round, flat and spread (Fig. 1A). Using the program CellProfiler, we quantified aspects of cellular morphology from label-free ptychographic images and revealed a significantly larger length:width ratio in Y201 versus Y202 BMSCs (3.59 ± 0.072 vs. 2.016 ± 0.051, mean ± SD, $p < 0.0001$), whereas Y202 cells had an increased average cell area ($p < 0.0001$) versus Y201 cells (Fig. 1B and C). We also observed differences in migratory phenotype, visualised in rose plots generated by tracking individual cells (Fig. 1D) with Y201 cells moving nearly twice as far and more quickly on average ($p < 0.0001$) (Fig. 1E and F).

To determine whether differences in cell morphology correlated with cytoskeletal variations, we fluorescently labelled focal adhesions (FA) and actin in Y201 and Y202 BMSCs (Fig. 1G). Phalloidin staining revealed criss-crossing actin networks in Y202 cells whereas Y201 appeared to have more aligned actin fibres. Quantification of FA size revealed that FAs in Y202 cells displayed a significantly increased mean area of 1.572 μm^2 versus 1.164 μm^2 per adhesion in Y201 (Fig. 1H). As well as increased area per-adhesion, Y202 also had significantly more adhesions on average (Fig. 1I). Senescent BMSCs have morphology and differentiation characteristics similar to Y202 cells. To determine if Y202 BMSCs displayed features associated with senescence, we performed a beta galactosidase assay. No staining was identified in either cell line at 24 h (data not shown). At 72 h, 0% and 16% of Y201 and Y202 cells respectively were positive for beta-galactosidase (Fig. S1A). When we examined our previously published microarray data [22] there was no discernible pattern of expression of numerous senescence associated genes in Y201 and Y202 cells (Fig. S1B). Our previous studies also provide detailed evidence for a Y202-like phenotype in primary BMSC cultures [24], therefore these data suggest strongly that Y202 behaviour is not indicative of a senescent population. However, this does raise interesting avenues for further study in the association between inflammation, senescence and cellular function and phenotype. We confirmed the presence of Y201-like and Y202-like populations in CFU-F cultures of primary BMSCs by building an analysis pipeline that could distinguish and classify cells based upon morphological phenotypes. Using the CellProfiler pipeline we identified contrasting phenotypes within the same culture of primary cells, including cells with Y201-like fibroblastic morphologies and Y202-like, flattened and spread morphologies (Fig. 1J). Image analysis of three separate primary cultures nominally identified 48.5% of cells in primary cultures as “Y201” and 24.7% as “Y202” (Fig. 1K). The remaining 26.1% was designated as unclassified, having a morphology somewhere between the two defined populations. We conclude that morphologically and functionally-distinct cell subsets co-exist in BMSC populations.

Secreted factors from Y201 BMSCs drive phenotypic switching in Y202 BMSCs

We hypothesised that the BMSC phenotype is plastic and at least in part regulated by the interactions of clonally-derived cell subtypes to determine the overall function of the population. We used the unique, quantifiable features of Y201 and Y202 cell lines as a model of BMSC heterogeneity to test this hypothesis. To determine the role of secreted factors on phenotype maintenance, we transferred conditioned media (CM) between Y201 and Y202, and monitored cell morphology and migration in CFU-F assays, focusing on the effects of the Y201 secretome on behavioural changes in atypical Y202 stromal cells. The varied morphology and inherent migration of some BMSC subtypes makes quantifying metrics from CFU-F assays complex. To overcome this, we developed a CellProfiler pipeline capable of accurately identifying colonies of various morphologies from scanned images of crystal violet stained CFU-F assays (Fig. S1C). Exposure of Y202 cells to Y201-CM resulted in a significant increase in colony size compared to their own Y202-CM, and no conditioned media treated colonies ($p = 0.0157$ and $p = 0.0018$ respectively) (Fig. 2A and B). This increase in colony size appeared to arise from increased migration of cells resulting in colony spreading from the initiation point.

To quantify the effect of Y201-CM on Y202 cell migration further, we used a ptychographic imaging technique to track individual cells within colonies over time.

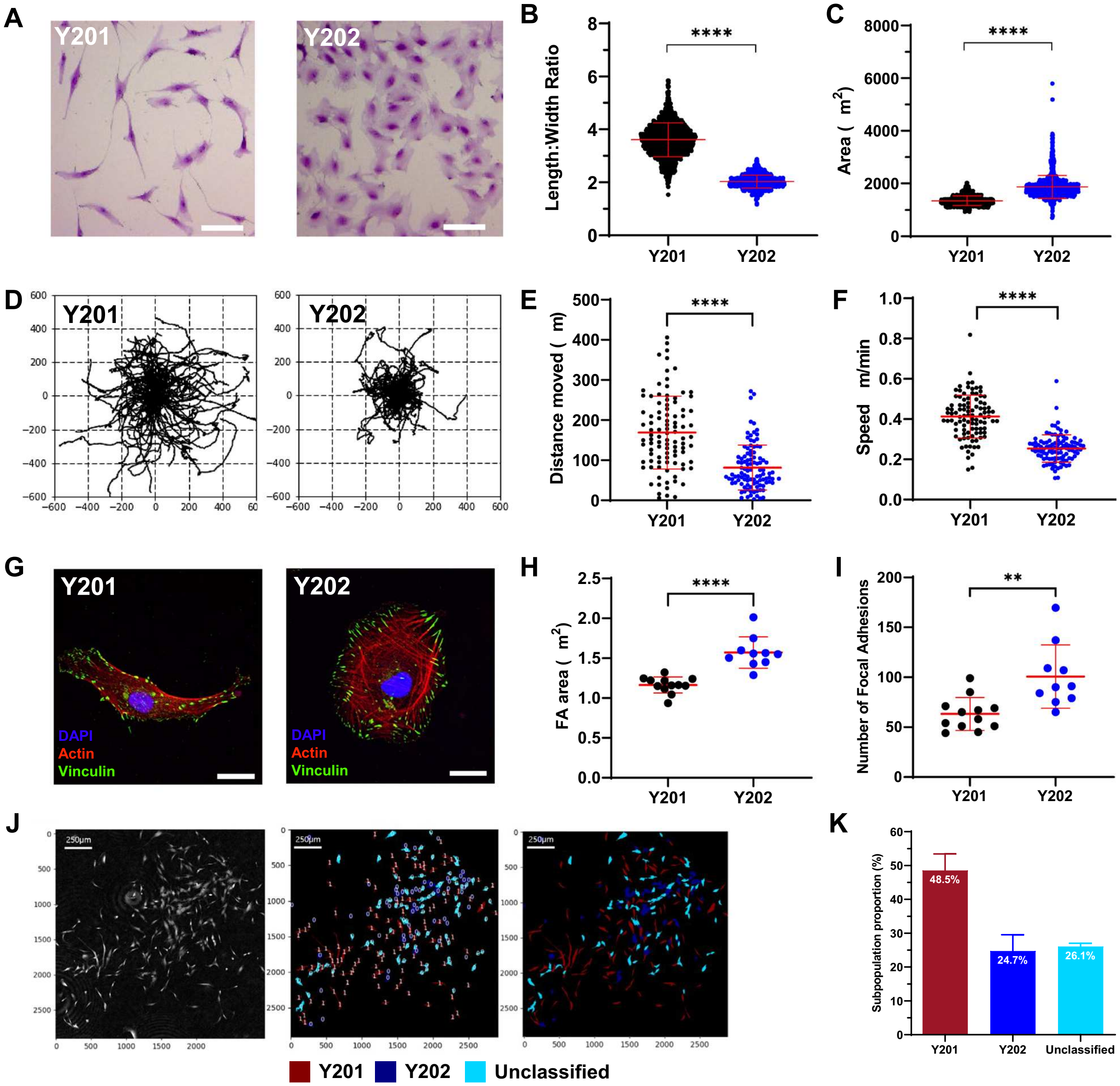

Fig. 1 Image analysis of morphologies and migratory phenotypes in Y201 and Y202 BMSCs. **A** Y201 and Y202 stromal cell subtypes stained with crystal violet and imaged by brightfield microscopy (scale bar = 50 µm). **B** Length:width ratios quantified from still frames from ptychographic images of Y201 and Y202 (*T*-test, $P < 0.0001$, n = 2418). **C** Cell area quantified from still frames from ptychographic images of Y201 and Y202 (*T*-test, $p < 0.0001$, n = 2418). **D** Rose-plots showing migratory profiles of Y201 and Y202 BMSCs. **E**, **F** Quantification of migratory characteristics of Y201 and Y202 from ptychographic live-cell tracking. **G** Representative immunofluorescence images of Y201 and Y202 cells showing focal adhesions (vinculin, green), actin (phalloidin, red) and nuclei (DAPI, blue), scale bar = 20 µm **H** Quantification of fluorescence images for mean focal adhesion (FA) area of Y201 versus Y202 (n = 10–12) **I** Number of focal adhesions per cell from Y201 and Y202 cells. **J** Ptychography was used to build a CellProfiler pipeline that could classify primary cell populations based upon Y201 and Y202 morphological metrics. Representative images show phase-contrast images in the first frame which are overlayed to represent the classification of primary BMSCs. Red = Y201-like subtypes, blue = Y202-like subtypes, light-blue = unclassified. **K** Quantification of Y201 and Y202-like subtypes identified in primary BMSC populations, all error bars = Mean ± SD. *$p \leq 0.05$, **$p < 0.01$, ***$p < 0.001$, ****$p < 0.0001$

From time-lapse imaging we observed that Y202 cells became more dispersed and elongated following exposure to Y201-CM compared with Y202-CM controls (Supplementary videos 1 and 2). In quantitative analyses we demonstrated that Y202 cells underwent morphological changes following exposure to Y201-CM, with

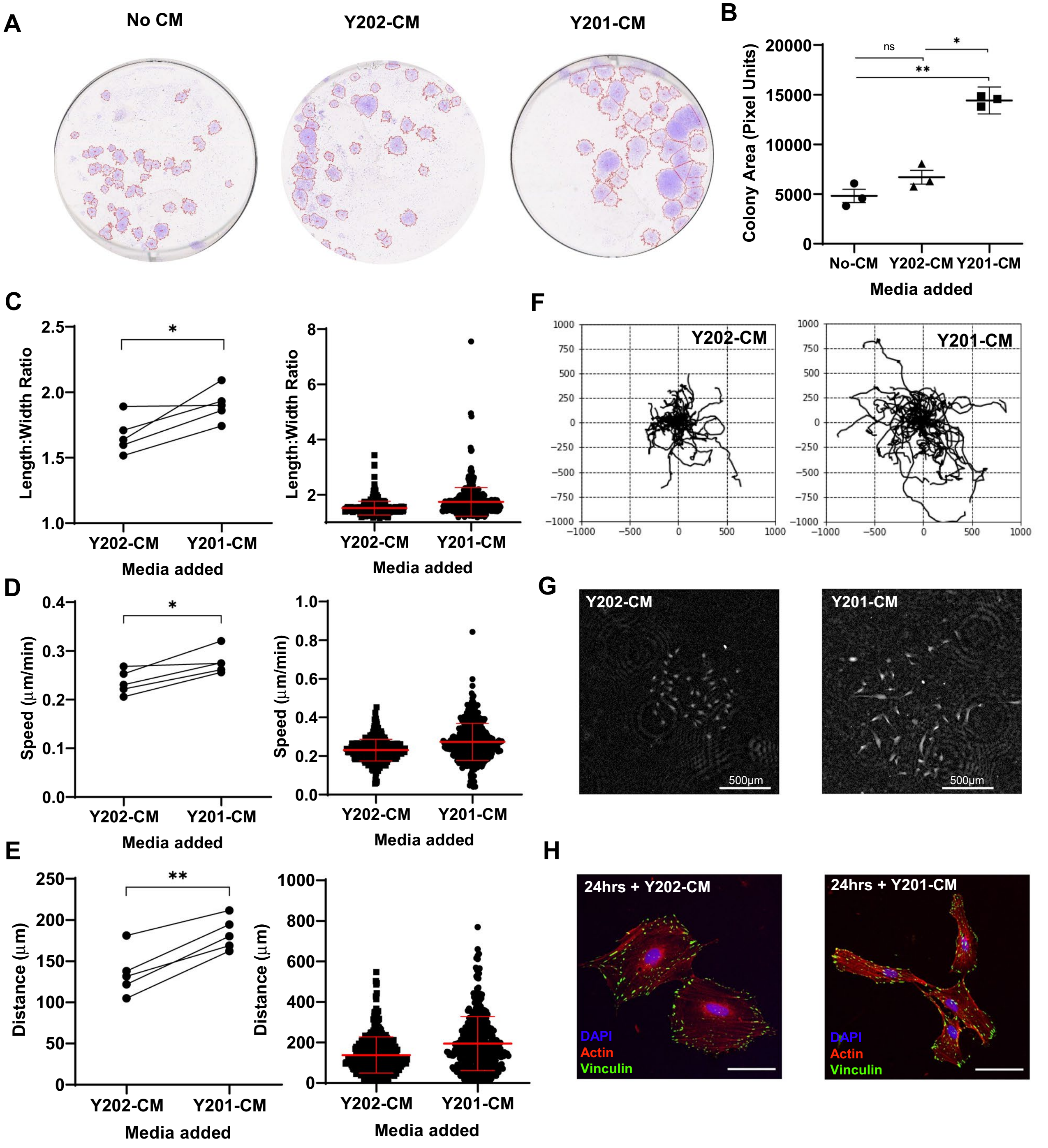

Fig. 2 Effect of Y201 secreted factors on morphology and migration of Y202 cells. **A** Representative images of crystal violet stained CFU-F cultures of Y202 grown in either unconditioned medium (no CM), Y201-conditioned medium or Y202-conditioned medium showing gross colony morphology. **B** Mean colony area of Y202 colonies treated with various conditioned media (ANOVA: $F = 60.05$, $df = 1.12, 2.26$, $p = 0.0113$). **C** Mean length:width ratio from a single experiment (left) and multiple repeats (right) ($n = 5$). **D** Speed of mean cell movement from a single experiment and the mean speed from multiple repeats ($n = 5$). **E** Displacement distance of cells from tracking origin for a single experiment and the mean distance from multiple repeats ($n = 5$). **F** Rose-plots of cell migratory pathways after exposure to Y201 or Y202 conditioned media. **G** Phase contrast image of typical colonies at assay endpoint. **H** Representative immunofluorescent images of Y202 cells treated with either Y201-CM or Y202-CM for 24 h with focal adhesions (vinculin, green), actin (phalloidin, red) and nuclei (DAPI, blue), scale bar = 20 μm. $*p \leq 0.05$, $**p < 0.01$, ns = not significant. Error bars ± SEM

a significant increase in length:width ratio ($p = 0.0293$) (Fig. 2C). Similarly, we found significant increases in migration speed ($p = 0.0141$) and displacement distance ($p = 0.0012$) for Y202 cells treated with Y201-CM versus Y202-CM (Fig. 2D and E). Rose-plots from individually tracked cells illustrate the increased migration of Y202 cells with exposure to Y201-CM (Fig. 2F) with examples of colonies at the assay endpoint shown in Fig. 2G. By fluorescent staining we observed a change in morphology of Y202 cells to a more elongated Y201-like phenotype within 24 h of exposure to Y201-CM (Fig. 2H), however, we saw no significant change in the size of focal adhesions between Y202-CM and Y201-CM treatments ($p = 0.46$) (Fig. S2A). The mean focal adhesion size of Y202-CM (1.323 μm^2, n = 16) and Y201-CM (1.395 μm^2, n = 17) treated cells was notably between the sizes of the highly migratory Y201 and less migratory Y202 (1.572 μm^2 and 1.164 μm^2 respectively, shown in Fig. 1H).

We repeated this CFU-F assay using in vitro-aged (> 10 passages) primary BMSCs, which typically display reduced CFU-F activity compared to low-passage cells. We found that primary in vitro aged cells exposed to Y201-CM increased the number of colonies, albeit not significantly ($p = 0.0738$), but the subsequent colonies grew significantly larger than unconditioned media controls ($p = 0.0133$) while Y202-CM had no significant effect over standard culture conditions (Fig. S2B and C). In one donor (K136), Y201-CM completely restored colony forming capacity.

BMSC heterogeneity is reflected in variability of secreted factors

Having determined that exposure to Y201 secreted factors was able to drive changes in morphology and migration of Y202 cells, we interrogated the secretomes of these cell subsets using LC–MS/MS of CM. Remarkably, all 861 proteins detected were expressed by both Y201 and Y202 BMSC subtypes. From this we identified 44 and 129 proteins with significantly increased expression in Y201 and Y202 BMSCs respectively ($p < 0.05$) (Fig. 3A). Using the cell region-based rendering and layout tool in cytoscape we confirmed the majority of our differentially expressed proteins have been annotated as appearing in the extracellular space (Fig. 3B). The 44 proteins significantly elevated in Y201 versus Y202 are shown in Fig. 3C ranked by normalised abundance. The most highly abundant proteins with significant fold changes were predominantly ECM components (e.g. FN1, COL6A1, BGN, DCN, THBS1), with notable elevated levels of periostin (POSTN) and aggrecan (ACAN) (71- and 104-fold higher than Y202 respectively, Fig. 3C arrows). Conversely, Lumican (LUM) was the most upregulated ECM component in Y202 cell secretome with levels 9.7-fold higher than Y201 cells (Fig. S3A). KEGG pathway enrichment of significantly upregulated proteins revealed strong correlation for Y201 secreted proteins in the 'ECM-Receptor Interaction' and 'Focal Adhesion' pathways while Y202 upregulated proteins demonstrated weak but significant correlation with the 'Lysosome' and various metabolic pathways (Fig. 3D).

The recurring references to ECM in KEGG pathway enrichment was investigated further by comparing all proteins identified in LC–MS/MS of Y201 and Y202 secretome against the matrisome, a curated database of human proteins known to contribute to or associate with ECM through either structure, interaction, or regulation [37]. From 861 proteins identified in the secretome, 175 (20.3%) were annotated in the matrisome, with 85 labelled as "core matrisome" and 90 as "matrisome associated" (Fig. 3E). Chi-squared tests revealed significant enrichment for matrisome proteins (28 observed versus 8.9 expected) in the Y201 secretome ($\chi^2 = 50.97$, $df = 1$, $p < 0.0001$). Notably, Y202 significantly upregulated proteins did not differ significantly from expected amounts ($\chi^2 = 0.1576$, $df = 1$, $p = 0.69$). Of the 175 matrisome proteins in the total secretome, 122 proteins did not differ significantly between Y201 and Y202 (Fig. S3B).

Secreted ECM products from Y201 are identified in CD271-positive microenvironments in vivo

We used the ECM proteins identified in the secretomic screen as candidate markers of a Y201-like stromal cell microenvironment. Using immunofluorescent labelling we identified expression of four ECM proteins differentially upregulated by Y201 BMSCs (collagen-VI, biglycan, aggrecan and periostin) in sections of mouse and human bone. All four ECM proteins were found lining trabecular bone, in addition networks of collagen-VI were also identified throughout the marrow (Fig. 4A and B). Very similar distribution patterns for all four were observed in mouse bone (Fig. S4). The level of periostin and aggrecan in endosteal regions of mouse bone was considerably lower than that found in periosteum while aggrecan was considerably less than that found in hypertrophic cartilage.

We further investigated the distribution of periostin and aggrecan having identified these as the most differentially expressed proteins in Y201 secretome. We immunostained for CD271, one of the markers identified for appropriate selection and enrichment of colony forming human BMSCs that demonstrated tripotent differentiation in vitro [38, 39]. We identified CD271-positive staining in bone-lining regions in all tested donors with evidence for both aggrecan and periostin adjacent to the basal surfaces of these cells (Fig. 4C and D). Some aggrecan immunostaining was identified

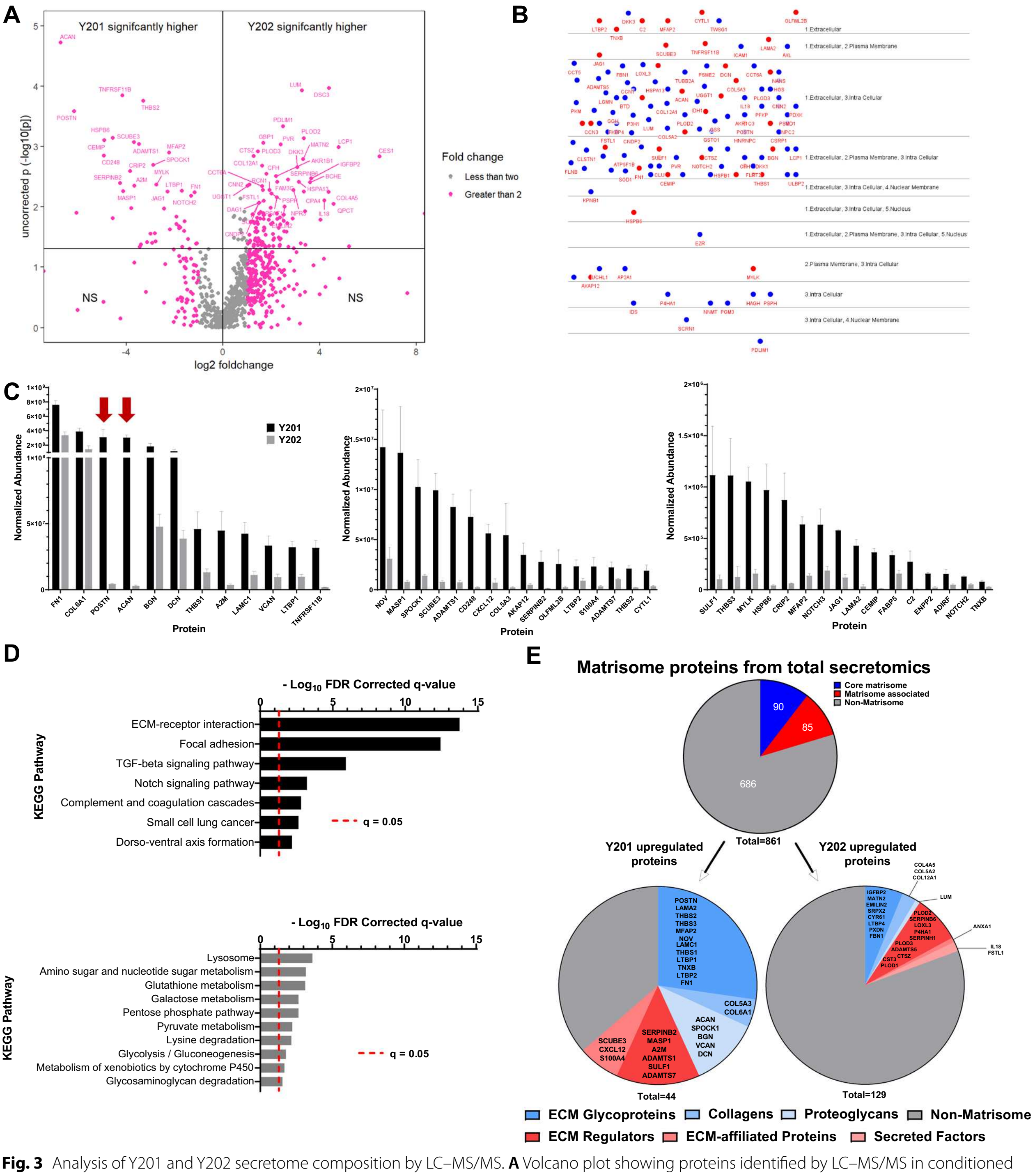

Fig. 3 Analysis of Y201 and Y202 secretome composition by LC–MS/MS. **A** Volcano plot showing proteins identified by LC–MS/MS in conditioned media from Y201 and Y202 cells. Proteins identified as significantly enriched by ANOVA n = 3, $p < 0.05$ are shown in upper quadrants. **B** CEREBRAL layout of significantly differently expressed proteins from Y201 (red) and Y202 (blue) showing the majority have been annotated as found in the extracellular space and are likely secreted. **C** Significantly enriched proteins secreted by Y201 versus Y202 represented in order of overall normalised abundance from LC–MS/MS. Graphs have been split for ease of interpretation while maintaining a linear scale, red arrows indicate POSTN and ACAN, error bars are means ± SEM. **D** KEGG pathway analysis of significantly upregulated proteins in Y201 (top) and Y202 (bottom). **E** All identified secreted proteins were annotated using the matrisome database (top) and categorized as "core matrisome" (blues), "matrisome-associated" (reds) and "non-matrisome" (grey). Significantly enriched proteins from secretomics for Y201 (left) and Y202 (right) are shown with matrisome annotations in the respective subcategories listed

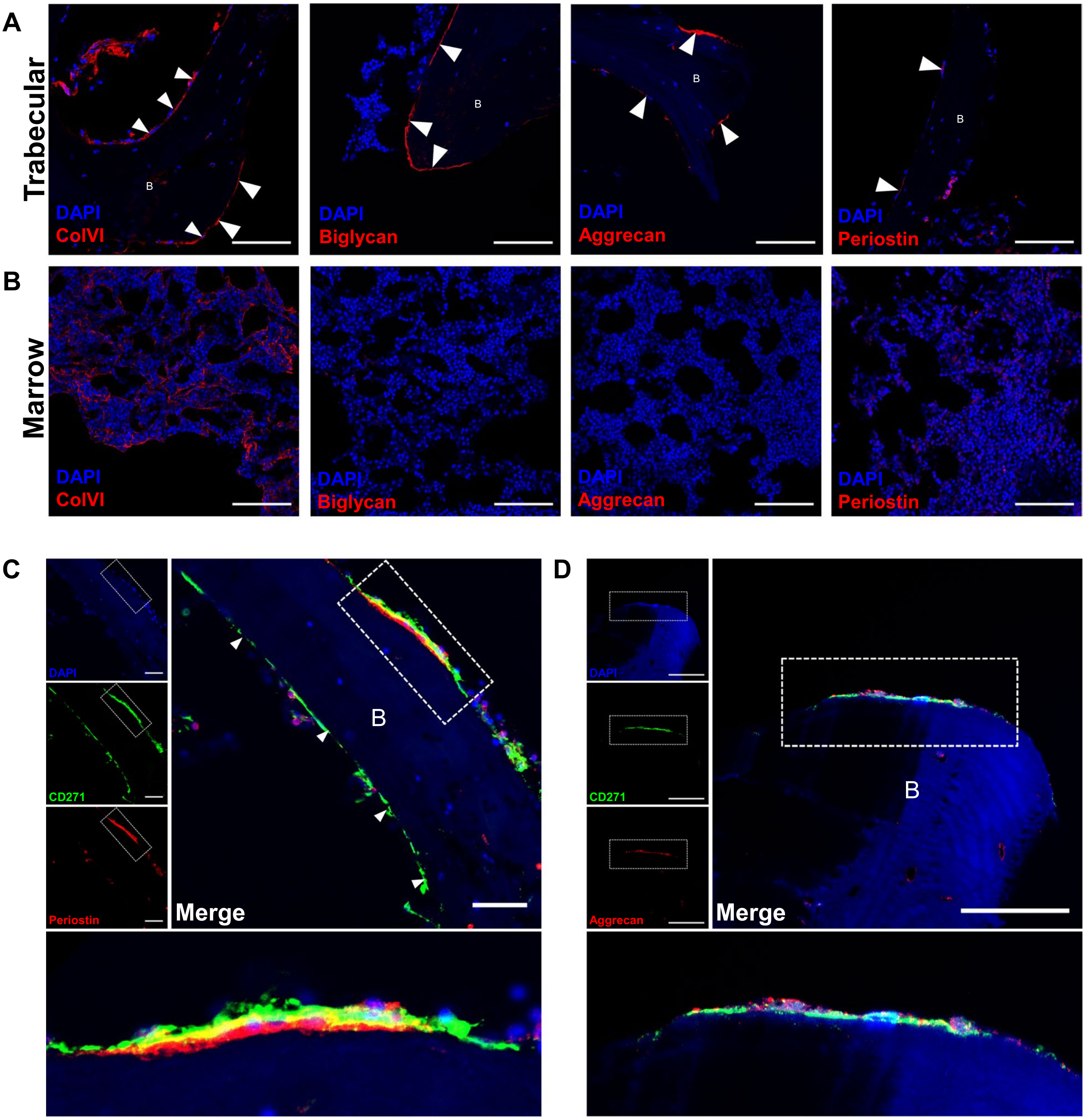

Fig. 4 Immunofluorescent imaging of human bone marrow to identify Y201 BMSC-associated ECM proteins. **A** regions of human trabecular bone with fluorescently labelled nuclei (blue, DAPI) and ECM proteins (Red, AF568), scale bar = 100 µm. Arrows show where ECM expression is identified in bone lining regions. **B** regions of human marrow with fluorescently labelled nuclei (blue, DAPI) and ECM proteins (Red, AF568), scale bar = 100 µm. **C** CD271 (green, AF488) and periostin (red, AF568) co-localisation in a bone-lining region with nuclei (blue, DAPI). individual channel images are shown. Dashed rectangle is shown as expanded view (bottom), scale bar = 50 µm. **D** CD271 (green, AF488) and aggrecan (red, AF568) co-localisation in a bone lining region with nuclei (blue, DAPI), individual channel images are shown. Dashed rectangle is shown as expanded view (bottom), scale bar = 50 µm. B = trabecular bone

associated with vessel-like structures within compact bone, which may be linked to Haversian remodelling, but more in-depth analyses would be needed to confirm this observation. It should also be noted that not all endosteal lining CD271-positive cells were found adjacent to periostin and aggrecan, indicating that these proteins may be expressed by a limited subset of BMSCs.

Stromal extracellular matrix substrates regulate migratory and morphological phenotype

To determine how differences in ECM composition identified in the LC–MS/MS analysis influenced ECM organisation, we examined the matrix substrate deposited by Y201 and Y202. Y201 and Y202 BMSCs were cultured for 2 weeks to allow deposition of a layer of ECM onto the cell culture surface. After removal of the cell layer we used SEM to examine the topographical features of the matrices (Fig. 5A). The matrix made by Y201 appeared to be more compact with larger and potentially deeper undulations. In contrast the matrix produced by Y202 cells appeared flattened, with fibres visible at both high and low magnifications (Fig. 5A). Differences in the organisation of Y201 and Y202 matrices was also demonstrated by FIB-SEM. The overall architecture of the ECM was apparent when observed at low magnification prior to initial FIB-SEM experiments. Y201 ECM appeared as a consistent mat of dense fibres whereas Y202 ECM presented as a more disperse meshwork with irregular patches of more fibrous matrix (Fig. 5B). FIB-SEM was used to section through and image the ECM, revealing that ECM produced by Y201 cells was notably thicker than that produced by Y202 cells (Fig. 5B).

ECM deposited by BMSC subtypes appeared structurally distinct and so we hypothesised that this may explain the different morphological and migratory patterns of the producing cells. However, unlike soluble factors present in CM (See Fig. 2), ECM substrates from both Y201 and Y202 cells increased migration and elongation of Y202 cells compared to those cultured on plastic. Y202 cells cultured on Y201 ECM and their own ECM became more fibroblastic as shown by the increased length:width ratio (Fig. 5Ci). Y202 cells cultured on both ECMs also migrated further from their point of origin and at an increased speed versus Y202 cells grown on plastic (Fig. 5Cii and iii). Considering these observations, we investigated whether the presence of particular ECMs could influence the differentiation of nullipotent Y202 BMSCs. We demonstrated that both Y201 and Y202 ECM substrates enhanced the rate and quantity of calcification by Y201 cells as shown by enhanced alizarin red staining (Fig. S5). We also saw evidence of increased osteogenic differentiation by Y202 cells when cultured on either ECM compared to a complete lack of osteogenic differentiation when cultured on plastic.

Finally we tested the role of focal adhesion kinase (FAK) in ECM-mediated changes in migration. The FAK inhibitor (FAKi) (PF573228) did not significantly alter the length:width ratio of Y202 cells cultured on Y201 ECM at any concentration tested (Fig. 5Di) but did significantly reduce the mean migration speed (at 10 μM FAKi) and the displacement of individual cells from their starting point Y202 cells treated (at 3 and 10 μM FAKi) (Fig. 5Dii–iii).

Discussion

Our findings provide further evidence of a correlation between BMSC morphology and functionality, supporting previous evidence that morphologically distinct stromal subsets are likely to reflect functional heterogeneity, and observations that cells with different morphologies have altered inflammatory or differentiation characteristics [19, 40–43]. We exploited a label-free ptychographic technique to track the morphology and motility of cells over time [44]. This could prove useful in the real-time discrimination of primary cell population phenotypes without the need for fluorescence-based or other endpoint labelling methods. Using our simplified model of BMSC heterogeneity we showed that large, flat, inflammatory BMSCs were less motile than stem cell-like, spindle-shaped cells. In addition, cells matching these morphological parameters were reproducibly observed in primary cultures, suggesting that image-based morphometric analysis could be employed as a predictive measure of cell function, with previous evidence suggesting faster migrating BMSCs are indeed more likely to be multi-potent [45]. Furthermore, we demonstrated that morphometric features of the atypical flattened BMSCs (Y202) were plastic and could be modified by exposure to factors secreted by more typical, spindle-shaped Y201 BMSCs. BMSC phenotypic plasticity may be, to some extent, determined by the secreted factors of the cell population as a whole, with ECM components being important determinants of cell behaviour.

The BMSC secretome is linked to cellular functionality, which is important both for the understanding of disease and potential uses of these cells in therapies [46]. We found that the secretome of multipotent Y201 BMSCs was strongly enriched for proteins involved in the production and modification of the ECM, as well as TGF-beta and Notch signalling pathways both of which are implicated in controlling BMSC differentiation [47, 48]. Subsequent assessment of the ECM produced by these BMSC lines identified a thicker and more complex matrix produced by Y201 cells, while Y202-derived matrices were relatively thin. The influence of surface topography and stiffness has been demonstrated to be of fundamental importance for maintenance of stemness in BMSCs [49]. We acknowledge that our technique for generating the ECM may alter some nano-scale topography while maintaining overall integrity. The different matrices produced are likely have unique biomechanical properties and the forces experienced by a cell such as stiffness are likely linked to the microenvironmental ECM composition which can have dramatic implications for BMSC

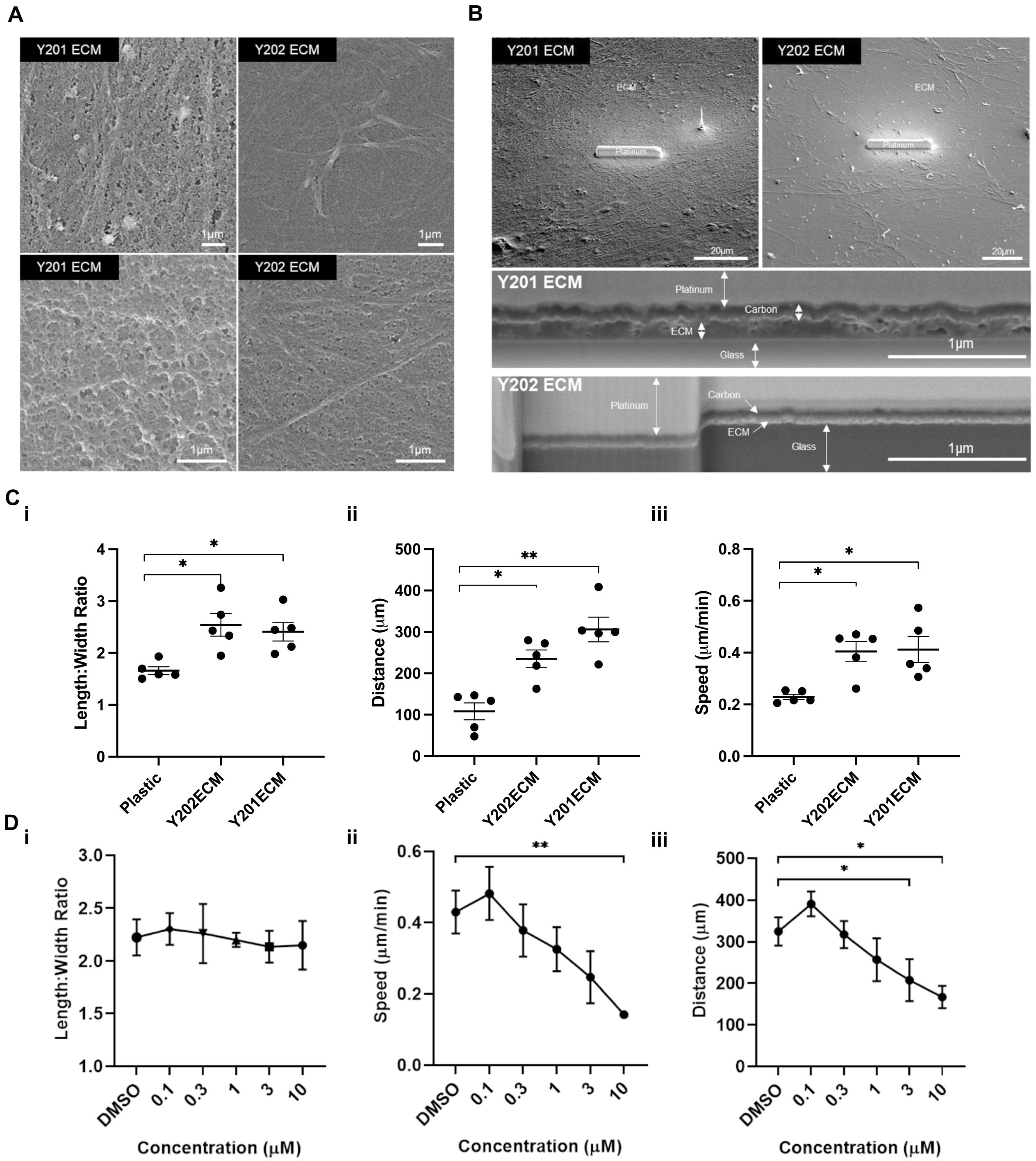

Fig. 5 Effect of ECM substrates derived from Y201 BMSCs on Y202 BMSC migration. **A** Scanning electron micrographs of Y201 and Y202 extracellular matrices after 2 weeks in culture. **B** Scanning electron micrograph of expanded view of Y201 and Y202 extracellular matrices with platinum strip laid to protect sample during Focused Ion Beam (FIB) milling. Bottom panels indicate side view after FIB milling revealing cross-section view of matrix deposition. **C** Mean (i) length:width ratio, (ii) speed and (iii) distance travelled of Y202 cells cultured on tissue culture plastic, Y202 ECM or Y201 ECM (n = 5 experiments). **D** Mean (i) length:width ratio, (ii) speed and (iii) distance travelled of Y202 cells cultured on Y201 ECM with various concentrations of FAK inhibitor (PF573228) n = 4 experiments. $^{*}p \leq 0.05$, $^{**}p < 0.01$, $^{***}p < 0.0001$. Error bars ± SEM

fate and even immune responses [50, 51].The increased detection of periostin in the ECM of Y201 is interesting given its acknowledged role in increasing crosslinking of collagens resulting in stiffer ECM [52, 53]. The ECM has a prominent role in driving migration, and as such the increased production and secretion of matrix proteins captured in conditioned media could contribute to the phenotypic switch we saw in Y202 cells. Lumican, which was secreted at higher levels by Y202 cells, has previously been shown to inhibit the migration of MSCs, as well as regulation of immune responses in other cell types, potentially correlating with the slow moving immune-based role of Y202 [54].

Similarly, aggrecan and periostin were more abundantly secreted by Y201 BMSCs compared to Y202 BMSCs, and may act as candidate differentiators of cell phenotype. It is also possible that the 122 proteins that did not differ significantly between the two BMSC lines represent a 'core' matrix common to all, and important for shared functions, across BMSC subtypes. The ECM is undoubtedly important for cellular function, mediating biochemical and mechanical signals to cells. Molecular patterning of a niche environment has previously been shown to regulate macrophages between a pro-healing and inflammatory phenotype [55]. This is likely to be of high importance for stem cells in a structurally diverse tissues such as bone marrow, where the role of ECM in maintaining hematopoietic stem cells in their niche has been increasingly characterised [56, 57]. Our identification of aggrecan and periostin underlying some CD271$^+$ cells in human bone marrow provides promising evidence that an in vitro matrix produced by cells isolated from a complex tissue may, at least in part, recapitulate the in vivo ECM composition of the stromal microenvironment. The expression of aggrecan mRNA, a typical chondrocyte marker, by BMSCs has previously been reported and aggrecan immunostaining was recently identified by others in endosteal regions associated with a skeletal stem cell population displaying an osteoblast-chondrocyte transitional identity [58, 59]. We speculate that the expression of aggrecan in bone lining regions and by more migratory MSCs may be indicative of an ability for these cells to "respond" to trauma and contribute to periosteal chondrogenesis and fracture healing [60]. Our findings are supported by previous evidence for CD271$^+$ BMSC microenvironments, with CD271$^+$CD56$^+$ cells found exclusively on trabecular bone surfaces, representative of an endosteal BMSC niche [61, 62]. CD271$^+$ BMSCs are also 65-fold increased in BMSCs isolated from trabeculae versus bone marrow aspirates, again highlighting a more endosteal microenvironment for this population [63]. The same pattern of CFU-F capacity and in situ localisation is seen when combined with another prospective potency marker, melanoma cell adhesion molecule (MCAM/CD146), as CD271$^+$CD146$^{-/low}$ populations were found as bone lining cells, whereas CD271$^+$CD146$^+$ were located perivascularly [64]. We hypothesise that differentiation-competent cells pattern their local environment with a phenotype-supportive matrix that is physically and biochemically suited to cell function, with our findings complementing other studies showing that matrix of young MSCs has been shown to restore proliferation and differentiation to older MSCs which has important implications for downstream therapeutic development [65–67].

Periostin has previously been linked with controlling the regenerative potential of periosteal skeletal stem cells, as well as supporting haematopoietic stem cells in the foetal liver niche and regulating their quiescence [68, 69]. The observation of rare endosteal periostin in bone marrow has not been previously reported in large-scale analyses of protein distribution across whole long-bones, however BMSC-derived periostin has also been shown in mouse to have functional effects in leukaemia, suggesting it is present in marrow [69–71]. Further, periostin knockdown in human BMSCs results in inhibition of osteogenic differentiation of these cells, indicating its importance for a differentiation-competent, stem cell phenotype [72]. The observation of periostin and aggrecan expression in trabecular bone regions in mouse and human tissue sections might also indicate conservation across species for these proteins in a stromal microenvironment for bone lining cells. Where cell-surface markers have proved unsuccessful in identifying sufficiently specific functional populations of BMSCs for therapeutic purposes there is a potential that this could be combined with functional assessment of secreted factors and/or the ECM that the cells produce. Follow up work to isolate CD271+ aggrecan and periostin-expressing primary BMSCs is necessary to determine if these possible biomarkers of potency are consistent and selective.

We demonstrated that the ECM substrate produced by both potent and nullipotent BMSCs may restore a migratory phenotype. In contrast to the effects of CM, where soluble factors produced by Y201 cells significantly increased Y202 cell elongation and migration compared to Y202 CM, growing Y202 on either Y201 or Y202 ECM substrates induced a Y201 morphometric phenotype in Y202 cells. These findings highlight important differences in how secreted factors and matrix substrates influence cell behaviour. It may be that core matrisome proteins, those shared by both cell-lines, are able to coordinate the phenotype of the attached cells, which is prevented by initial attachment to plastic. Furthermore, the increased migration, speed and distance-travelled of Y202 BMSCs grown on Y201 ECM occurred in a FAK-dependent manner, demonstrating the importance of cell–matrix interactions in this process.

Conclusions

In summary, we have demonstrated that there is a complex interplay between stromal cell subtypes that exhibit phenotypic plasticity driven by secreted signals, with the ECM playing a prominent role. As a result, the ECM will contribute to the initiation, maintenance and resolution of cellular heterogeneity. A stable and consistent ECM, for example at specific anatomical microenvironment in vivo, can also contribute to phenotypic stability.

Abbreviations

BMSC	Bone marrow stromal cell
ECM	Extracellular Matrix
ACAN	Aggrecan
CFU-F	Colony forming unit fibroblastic
CM	Conditioned media
DMEM	Dulbecco's modified eagle medium
FA	Focal adhesion
FAK	Focal adhesion kinase
FBS	Foetal bovine serum
FDR	False discovery rate
FIB-SEM	Focused ion beam scanning electron microscopy
hTERT	Human telomerase reverse transcriptase
KEGG	Kyoto Encyclopedia of Genes and Genomes
LEPR	Leptin receptor
OCT	Optimal cutting temperature compound
POSTN	Periostin
SEM	Scanning electron microscopy

Supplementary Information

The online version contains supplementary material available at https://doi.org/10.1186/s13287-024-03786-1.

Supplementary Figure 1: **A** Quantification of senescence associated beta-galactosidase staining at 72 hours. **B** Heatmap of microarray-derived data showing Log2 fold-change in expression of genes identified in the Reactome_senescence genes database in Y201 and Y202 compared to their parental cells. The classical senescence-associated genes CDKN1A, CCL2 and TP53 were not detected by the microarray and are not represented in the heatmap. **C** Outline of the CellProfiler pipeline for detection and quantification of crystal violet stained CFU-F assays. Supplementary Figure 2. **A** Quantification of focal adhesion size following fluorescent staining of Y202 cells treated with either Y201-CM or Y202-CM for 24 hours. **B** Mean colony area from in vitro aged primary BMSC CFU-Fs (n=5) (ANOVA: $F = 3.863$, $df = 1.833, 7.332$, $p = 0.0738$) **C** Total colonies identified from CFU-Fs of in vitro aged primary BMSCs (Friedman test, $p = 0.0085$) with post-hoc test revealing significant effect of Y201CM vs no CM ($p = 0.0044$) n = 5. $^*p \leq 0.05$, $^{***}p < 0.001$, ns = not significant. Error bars ± SEM. Supplementary Figure 3. **A** Significantly enriched proteins secreted by Y202 versus Y201 represented in order of normalised abundance from LC-MS/MS. Graphs are split for ease of interpretation while maintaining a linear scale, Means ± SEM. **B** Matrisome annotated proteins that were not significantly altered between Y201 and Y202 secretomes. Proteins are labelled as core-matrisome (blue) or matrisome-associated (red) with shading representing subcategories of these annotations. Supplementary figure 4. Representative immunofluorescence microscopy images of from n=4 mice various ECM proteins (violet) in mouse bone marrow with DAPI (blue) nuclear stain. Top row shows imaging of epiphyseal region of mouse femur. Middle row shows regions from the diaphysis of the femur. The bottom row shows isotype controls for respective stains. Expression along the endosteal surface is marked by closed arrowheads. Expression of protein around possible endothelial vessels is marked by open arrowheads. The line between compact bone and bone marrow in diaphysis regions is marked by a dotted line. * = cartilaginous/chondrocyte regions. Dense regions of DAPI staining in epiphysis and diaphysis regions marks marrow. Scale bars = 50 µm. Supplementary figure 5. Alizarin red staining for calcium deposition of osteogenic differentiation assays at day 0, 7, 14 and 21 for Y201 and Y202 cells cultured on plastic (left), Y201 ECM (middle) or Y202 ECM (right). Cells were treated with either osteogenic differentiation supplements (Osteo) or standard culture medium (Basal). Staining is representative of n=3 experiments.

Supplementary Table 1: Antibodies used for all immunofluorescence assays.

Supplementary Material 3.

Supplementary Material 4.

Acknowledgements
We thank staff at University of York Technology Facility for their help in performing the LC–MS/MS and for the use of the PhaseFocus Livecyte and confocal microscopes. We would also like to thank Adam Dowle of the York Centre of Excellence in Mass Spectrometry for assistance with all LC–MS/MS. We also thank Jon Barnard for his assistance with FIB-SEM at the York Nanocentre and Richard Kasprowicz for writing the code used to make the rose plots. We are also very grateful to the staff and patients from Clifton Park Hospital York for providing primary tissue from which BMSCs were extracted.

Author contributions

AS: conception and design, collection and assembly of data, data analysis and interpretation, manuscript writing and final approval of the manuscript. ER: collection and assembly of data, data analysis and interpretation, and final approval of the manuscript. GT: collection and assembly of data, data analysis and interpretation, and final approval of the manuscript. AK: collection and assembly of data, data analysis and interpretation, and final approval of the manuscript. AB: collection and assembly of data, data analysis and interpretation, and final approval of the manuscript. IH: conception and design, data interpretation, and final approval of the manuscript. PG: conception and design, data interpretation, manuscript writing, and final approval of the manuscript.

Funding
This work was funded by the Biotechnology and Biological Sciences Research Council United Kingdom, Doctoral Training Partnership grant (BB/M011151/1) and the Tissue Engineering and Regenerative Therapies Centre Versus Arthritis (21156). Instrumentation used is part of the York Centre of Excellence in Mass Spectrometry which was created thanks to a major capital investment through Science City York, supported by Yorkshire Forward with funds from the Northern Way Initiative, and subsequent support from engineering and physical sciences research council Grants (EP/K039660/1; EP/M028127/1).

Availability of data and materials

The proteomic datasets used and analysed in this article are available in the MassIVE repository (dataset identifier MSV000094888) ftp://massive.ucsd.edu/v08/MSV000094888/.

Declarations

Artificial intelligence

The authors declare that artificial intelligence was not used in this study.

Ethics approval

All work was approved by the University of York, Department of Biology Ethics Committee. Human femoral heads from routine hip and knee replacements were donated following informed consent from Clifton Park Hospital under ethical approval from the local NHS Research Ethics Committee and the University of York, Department of Biology Ethics Committee. Project titled "The influence of age, sex and disease on the number and quality of mesenchymal stem cells derived from bone marrow" (07/Q1105/9) approved 03/04/2007.

Consent for publication
Not applicable.

Competing interests
PG is co-founder and CSO for Mesenbio.

Author details
[1]Department of Biology, York Biomedical Research Institute, University of York, York, UK. [2]Brandeis University, Waltham, MA, USA.

Received: 2 October 2023 Accepted: 9 June 2024

References

1. Ding L, Saunders TL, Enikolopov G, Morrison SJ. Endothelial and perivascular cells maintain haematopoietic stem cells. Nature. 2012;481(7382):457–62.
2. Méndez-Ferrer S, Michurina TV, Ferraro F, Mazloom AR, Macarthur BD, Lira SA, et al. Mesenchymal and haematopoietic stem cells form a unique bone marrow niche. Nature. 2010;466(7308):829–34.
3. Caplan AI. Mesenchymal stem cells. J Orthop Res. 1991;9(5):641–50.
4. Pittenger MF, Mackay AM, Beck SC, Jaiswal RK, Douglas R, Mosca JD, et al. Multilineage potential of adult human mesenchymal stem cells. Science. 1999;284(5411):143–7.
5. Ghannam S, Bouffi C, Djouad F, Jorgensen C, Noël D. Immunosuppression by mesenchymal stem cells: mechanisms and clinical applications. Stem Cell Res Ther. 2010;1(1):2.
6. Sugiyama T, Kohara H, Noda M, Nagasawa T. Maintenance of the hematopoietic stem cell pool by CXCL12-CXCR4 chemokine signaling in bone marrow stromal cell niches. Immunity. 2006;25(6):977–88.
7. Choi H, Lee RH, Bazhanov N, Oh JY, Prockop DJ. Anti-inflammatory protein TSG-6 secreted by activated MSCs attenuates zymosan-induced mouse peritonitis by decreasing TLR2/NF-κB signaling in resident macrophages. Blood. 2011;118(2):330–8.
8. Wilson A, Hodgson-Garms M, Frith JE, Genever P. Multiplicity of mesenchymal stromal cells: finding the right route to therapy. Front Immunol. 2019;10:1112.
9. Wilson A, Webster A, Genever P. Nomenclature and heterogeneity: consequences for the use of mesenchymal stem cells in regenerative medicine. Regen Med. 2019;14(6):595–611.
10. Chan CKF, Gulati GS, Sinha R, Tompkins JV, Lopez M, Carter AC, et al. Identification of the human skeletal stem cell. Cell. 2018;175(1):43–56.
11. Chan Charles KF, Seo Eun Y, Chen James Y, Lo D, McArdle A, Sinha R, et al. Identification and specification of the mouse skeletal stem cell. Cell. 2015;160(1):285–98.
12. Liu Y, Chen Q, Jeong H-W, Koh BI, Watson EC, Xu C, et al. A specialized bone marrow microenvironment for fetal haematopoiesis. Nat Commun. 2022;13(1):1327.
13. Baryawno N, Przybylski D, Kowalczyk MS, Kfoury Y, Severe N, Gustafsson K, et al. A cellular taxonomy of the bone marrow stroma in homeostasis and Leukemia. Cell. 2019;177(7):1915–32.
14. Tikhonova AN, Dolgalev I, Hu H, Sivaraj KK, Hoxha E, Cuesta-Domínguez Á, et al. The bone marrow microenvironment at single-cell resolution. Nature. 2019;569(7755):222–8.
15. Wolock SL, Krishnan I, Tenen DE, Matkins V, Camacho V, Patel S, et al. Mapping distinct bone marrow niche populations and their differentiation paths. Cell Rep. 2019;28(2):302–11.
16. Kanazawa S, Okada H, Hojo H, Ohba S, Iwata J, Komura M, et al. Mesenchymal stromal cells in the bone marrow niche consist of multi-populations with distinct transcriptional and epigenetic properties. Sci Rep. 2021;11(1):15811.
17. Zhong L, Yao L, Tower RJ, Wei Y, Miao Z, Park J, et al. Single cell transcriptomics identifies a unique adipose lineage cell population that regulates bone marrow environment. Life. 2020;9:e54695.
18. Baccin C, Al-Sabah J, Velten L, Helbling PM, Grünschläger F, Hernández-Malmierca P, et al. Combined single-cell and spatial transcriptomics reveal the molecular, cellular and spatial bone marrow niche organization. Nat Cell Biol. 2020;22(1):38–48.
19. Klinker MW, Marklein RA, Lo Surdo JL, Wei C-H, Bauer SR. Morphological features of IFN-γ–stimulated mesenchymal stromal cells predict overall immunosuppressive capacity. Proc Natl Acad Sci. 2017;114(13):E2598–607.
20. Lee WC, Shi H, Poon Z, Nyan LM, Kaushik T, Shivashankar GV, et al. Multivariate biophysical markers predictive of mesenchymal stromal cell multipotency. Proc Natl Acad Sci. 2014;111(42):E4409–18.
21. Poon Z, Lee WC, Guan G, Nyan LM, Lim CT, Han J, et al. Bone marrow regeneration promoted by biophysically sorted osteoprogenitors from mesenchymal stromal cells. Stem Cells Transl Med. 2015;4(1):56–65.
22. James S, Fox J, Afsari F, Lee J, Clough S, Knight C, et al. Multiparameter analysis of human bone marrow stromal cells identifies distinct immunomodulatory and differentiation-competent subtypes. Stem Cell Rep. 2015;4(6):1004–15.
23. Dominici M, Le Blanc K, Mueller I, Slaper-Cortenbach I, Marini F, Krause D, et al. Minimal criteria for defining multipotent mesenchymal stromal cells. The International Society for Cellular Therapy position statement. Cytotherapy. 2006;8(4):315–7.
24. Kay AG, Fox JM, Hewitson JP, Stone AP, Robertson S, James S, et al. CD317-positive immune stromal cells in human “mesenchymal stem cell” populations. Front Immunol. 2022;13:903796.
25. de Jong MME, Kellermayer Z, Papazian N, Tahri S, Hofste Op Bruinink D, Hoogenboezem R, et al. The multiple myeloma microenvironment is defined by an inflammatory stromal cell landscape. Nat Immunol. 2021;22(6):769–80.
26. Ng CP, Mohamed Sharif AR, Heath DE, Chow JW, Zhang CBY, Chan-Park MB, et al. Enhanced ex vivo expansion of adult mesenchymal stem cells by fetal mesenchymal stem cell ECM. Biomaterials. 2014;35(13):4046–57.
27. Shao X, Taha IN, Clauser KR, Gao Y, Naba A. MatrisomeDB: the ECM-protein knowledge database. Nucleic Acids Res. 2019;48(D1):D1136–44.
28. Subramanian A, Tamayo P, Mootha VK, Mukherjee S, Ebert BL, Gillette MA, et al. Gene set enrichment analysis: a knowledge-based approach for interpreting genome-wide expression profiles. Proc Natl Acad Sci. 2005;102(43):15545–21550.
29. Liberzon A, Subramanian A, Pinchback R, Thorvaldsdóttir H, Tamayo P, Mesirov JP. Molecular signatures database (MSigDB) 3.0. Bioinformatics. 2011;27(12):1739–40.
30. Kanehisa M, Goto S. KEGG: Kyoto encyclopedia of genes and genomes. Nucleic Acids Res. 2000;28(1):27–30.
31. Shannon P, Markiel A, Ozier O, Baliga NS, Wang JT, Ramage D, et al. Cytoscape: a software environment for integrated models of biomolecular interaction networks. Genome Res. 2003;13(11):2498–504.
32. Wiggins L, Otoole PJ, Brackenbury WJ, Wilson J. Exploring the impact of variability in cell segmentation and tracking approaches. bioRxiv. 2023;54:155.
33. Schneider CA, Rasband WS, Eliceiri KW. NIH image to ImageJ: 25 years of image analysis. Nat Methods. 2012;9(7):671–5.
34. Carpenter AE, Jones TR, Lamprecht MR, Clarke C, Kang IH, Friman O, et al. Cell profiler: image analysis software for identifying and quantifying cell phenotypes. Genome Biol. 2006;7(10):R100.
35. Lamprecht MR, Sabatini DM, Carpenter AE. Cell profiler™: free, versatile software for automated biological image analysis. Biotechniques. 2007;42(1):71–5.
36. Dimri GP, Lee X, Basile G, Acosta M, Scott G, Roskelley C, et al. A biomarker that identifies senescent human cells in culture and in aging skin in vivo. Proc Natl Acad Sci U S A. 1995;92(20):9363–7.
37. Naba A, Clauser KR, Hoersch S, Liu H, Carr SA, Hynes RO. The matrisome: in silico definition and in vivo characterization by proteomics of normal and tumor extracellular matrices. Mol Cell Proteomics. 2012;11(4):M111.014647.
38. Jones EA, Kinsey SE, English A, Jones RA, Straszynski L, Meredith DM, et al. Isolation and characterization of bone marrow multipotential mesenchymal progenitor cells. Arthritis Rheum. 2002;46(12):3349–60.
39. Quirici N, Soligo D, Bossolasco P, Servida F, Lumini C, Deliliers GL. Isolation of bone marrow mesenchymal stem cells by anti-nerve growth factor receptor antibodies. Exp Hematol. 2002;30(7):783–91.
40. Waterman RS, Tomchuck SL, Henkle SL, Betancourt AM. A new mesenchymal stem cell (MSC) paradigm: polarization into a pro-inflammatory MSC1 or an immunosuppressive MSC2 phenotype. PLoS ONE. 2010;5(4):e10088.

41. Haasters F, Prall WC, Anz D, Bourquin C, Pautke C, Endres S, et al. Morphological and immunocytochemical characteristics indicate the yield of early progenitors and represent a quality control for human mesenchymal stem cell culturing. J Anat. 2009;214(5):759–67.
42. Neuhuber B, Swanger SA, Howard L, Mackay A, Fischer I. Effects of plating density and culture time on bone marrow stromal cell characteristics. Exp Hematol. 2008;36(9):1176–85.
43. Muraglia A, Cancedda R, Quarto R. Clonal mesenchymal progenitors from human bone marrow differentiate in vitro according to a hierarchical model. J Cell Sci. 2000;113(7):1161–6.
44. Marrison J, Räty L, Marriott P, O'Toole P. Ptychography—a label free, high-contrast imaging technique for live cells using quantitative phase information. Sci Rep. 2013;3(1):2369.
45. Bertolo A, Gemperli A, Gruber M, Gantenbein B, Baur M, Pötzel T, et al. In vitro cell motility as a potential mesenchymal stem cell marker for multipotency. Stem Cells Transl Med. 2015;4(1):84–90.
46. Chinnadurai R, Rajan D, Qayed M, Arafat D, Garcia M, Liu Y, et al. Potency analysis of mesenchymal stromal cells using a combinatorial assay matrix approach. Cell Rep. 2018;22(9):2504–17.
47. Indrawattana N, Chen G, Tadokoro M, Shann LH, Ohgushi H, Tateishi T, et al. Growth factor combination for chondrogenic induction from human mesenchymal stem cell. Biochem Biophys Res Commun. 2004;320(3):914–9.
48. Tezuka K-I, Yasuda M, Watanabe N, Morimura N, Kuroda K, Miyatani S, et al. Stimulation of osteoblastic cell differentiation by notch. J Bone Miner Res. 2002;17(2):231–9.
49. McMurray RJ, Gadegaard N, Tsimbouri PM, Burgess KV, McNamara LE, Tare R, et al. Nanoscale surfaces for the long-term maintenance of mesenchymal stem cell phenotype and multipotency. Nat Mater. 2011;10(8):637–44.
50. Engler AJ, Sen S, Sweeney HL, Discher DE. Matrix elasticity directs stem cell lineage specification. Cell. 2006;126(4):677–89.
51. Wong SW, Lenzini S, Cooper MH, Mooney DJ, Shin JW. Soft extracellular matrix enhances inflammatory activation of mesenchymal stromal cells to induce monocyte production and trafficking. Sci Adv. 2020;6(15):eaaw0158.
52. Sidhu SS, Yuan S, Innes AL, Kerr S, Woodruff PG, Hou L, et al. Roles of epithelial cell-derived periostin in TGF-β activation, collagen production, and collagen gel elasticity in asthma. Proc Natl Acad Sci. 2010;107(32):14170–5.
53. Norris RA, Damon B, Mironov V, Kasyanov V, Ramamurthi A, Moreno-Rodriguez R, et al. Periostin regulates collagen fibrillogenesis and the biomechanical properties of connective tissues. J Cell Biochem. 2007;101(3):695–711.
54. Malinowski M, Pietraszek K, Perreau C, Boguslawski M, Decot V, Stoltz JF, et al. Effect of lumican on the migration of human mesenchymal stem cells and endothelial progenitor cells: involvement of matrix metalloproteinase-14. PLoS ONE. 2012;7(12):e50709.
55. McWhorter FY, Wang T, Nguyen P, Chung T, Liu WF. Modulation of macrophage phenotype by cell shape. Proc Natl Acad Sci. 2013;110(43):17253–8.
56. Gattazzo F, Urciuolo A, Bonaldo P. Extracellular matrix: a dynamic microenvironment for stem cell niche. Biochim Biophys Acta. 2014;1840(8):2506–19.
57. Shen B, Tasdogan A, Ubellacker JM, Zhang J, Nosyreva ED, Du L, et al. A mechanosensitive peri-arteriolar niche for osteogenesis and lymphopoiesis. Nature. 2021;591(7850):438–44.
58. Mwale F, Stachura D, Roughley P, Antoniou J. Limitations of using aggrecan and type X collagen as markers of chondrogenesis in mesenchymal stem cell differentiation. J Orthop Res. 2006;24(8):1791–8.
59. Matsushita Y, Liu J, Chu AKY, Tsutsumi-Arai C, Nagata M, Arai Y, et al. Bone marrow endosteal stem cells dictate active osteogenesis and aggressive tumorigenesis. Nat Commun. 2023;14(1):2383.
60. Caron MMJ, Janssen MPF, Peeters L, Haudenschild DR, Cremers A, Surtel DAM, et al. Aggrecan and COMP improve periosteal chondrogenesis by delaying chondrocyte hypertrophic maturation. Front Bioeng Biotechnol. 2020;8:1036.
61. Ilas DC, Baboolal TG, Churchman SM, Jones WG, Giannoudis PV, Bühring H-J, et al. The osteogenic commitment of CD271+ CD56+ bone marrow stromal cells (BMSCs) in osteoarthritic femoral head bone. Sci Rep. 2020;10(1):11145.
62. Sivasubramaniyan K, Ilas DC, Harichandan A, Bos PK, Santos DL, de Zwart P, et al. Bone marrow-harvesting technique influences functional heterogeneity of mesenchymal stem/stromal cells and cartilage regeneration. Am J Sports Med. 2018;46(14):3521–31.
63. Jones E, English A, Churchman SM, Kouroupis D, Boxall SA, Kinsey S, et al. Large-scale extraction and characterization of CD271+ multipotential stromal cells from trabecular bone in health and osteoarthritis: Implications for bone regeneration strategies based on uncultured or minimally cultured multipotential stromal cells. Arthritis Rheum. 2010;62(7):1944–54.
64. Tormin A, Li O, Brune JC, Walsh S, Schütz B, Ehinger M, et al. CD146 expression on primary nonhematopoietic bone marrow stem cells is correlated with in situ localization. Blood. 2011;117(19):5067–77.
65. Marinkovic M, Dai Q, Gonzalez AO, Tran ON, Block TJ, Harris SE, et al. Matrix-bound Cyr61/CCN1 is required to retain the properties of the bone marrow mesenchymal stem cell niche but is depleted with aging. Matrix Biol. 2022;111:108–32.
66. Sun Y, Li W, Lu Z, Chen R, Ling J, Ran Q, et al. Rescuing replication and osteogenesis of aged mesenchymal stem cells by exposure to a young extracellular matrix. FASEB J. 2011;25(5):1474–85.
67. Block TJ, Marinkovic M, Tran ON, Gonzalez AO, Marshall A, Dean DD, et al. Restoring the quantity and quality of elderly human mesenchymal stem cells for autologous cell-based therapies. Stem Cell Res Ther. 2017;8(1):239.
68. Biswas A, Roy IM, Babu PC, Manesia J, Schouteden S, Vijayakurup V, et al. The periostin/integrin-αv axis regulates the size of hematopoietic stem cell pool in the fetal liver. Stem Cell Rep. 2020;15(2):340–57.
69. Duchamp de Lageneste O, Julien A, Abou-Khalil R, Frangi G, Carvalho C, Cagnard N, et al. Periosteum contains skeletal stem cells with high bone regenerative potential controlled by Periostin. Nat Commun. 2018;9(1):773.
70. Coutu DL, Kokkaliaris KD, Kunz L, Schroeder T. Three-dimensional map of nonhematopoietic bone and bone-marrow cells and molecules. Nat Biotechnol. 2017;35(12):1202–10.
71. Ma Z, Zhao X, Deng M, Huang Z, Wang J, Wu Y, et al. Bone marrow mesenchymal stromal cell-derived periostin promotes B-ALL progression by modulating CCL2 in Leukemia cells. Cell Rep. 2019;26(6):1533–43.
72. Han L, Gong S, Wang R, Liu S, Wang B, Chen G, et al. Knockdown of POSTN inhibits osteogenic differentiation of mesenchymal stem cells from patients with steroid-induced osteonecrosis. Front Cell Dev Biol. 2020;8:606289.

Publisher's Note